

Date of publication xxxx 00, 0000, date of current version xxxx 00, 0000.

Digital Object Identifier 10.1109/ACCESS.2020.DOI

Efficient 3-D Near-Field MIMO-SAR Imaging for Irregular Scanning Geometries

JOSIAH W. SMITH¹ AND MURAT TORLAK¹

¹Electrical and Computer Engineering, The University of Texas at Dallas, 800 W. Campbell Rd. Richardson, TX 75080 USA (e-mail: jws160130@utdallas.edu)

Corresponding author: Josiah W. Smith (e-mail: josiah.smith@utdallas.edu).

This work was supported by the Semiconductor Research Corporation (SRC) task 2712.029 through The University of Texas at Dallas' Texas Analog Center of Excellence (TxACE).

ABSTRACT In this article, we introduce a novel algorithm for efficient near-field synthetic aperture radar (SAR) for irregular scanning geometries. With the emergence of fifth-generation (5G) millimeter wave (mmWave) devices, near-field SAR imaging is no longer confined to laboratory environments. Recent advances in positioning technology have attracted significant interest in a diverse set of new applications for mmWave imaging. However, many use cases such as automotive-mounted SAR imaging, unmanned aerial vehicle (UAV) imaging, and freehand imaging with smartphones are constrained to irregular scanning geometries. Whereas traditional near-field SAR imaging systems and quick personnel security (QPS) scanners employ highly precise motion controllers to create ideal synthetic arrays, emerging applications, mentioned previously, inherently cannot achieve such ideal positioning. Additionally, many Internet of Things (IoT) and 5G applications impose strict size and computational complexity limitations that must be considered for edge mmWave imaging technology. In this article, we propose a novel algorithm to leverage the advantages of non-cooperative SAR scanning patterns, small form-factor multiple-input multiple-output (MIMO) radars, and efficient monostatic planar image reconstruction algorithms. We propose a framework to mathematically decompose arbitrary and irregular sampling geometries and a joint solution to mitigate multistatic array imaging artifacts. The proposed algorithm is validated in simulation and through an empirical study of arbitrary scanning scenarios. Our algorithm achieves high-resolution and high-efficiency near-field MIMO-SAR imaging and is an elegant solution to computationally constrained irregularly sampled imaging problems.

INDEX TERMS 5G, automotive SAR, drone mmWave imaging, freehand imaging, handheld scanner, irregular sampling, mmWave imaging, multistatic imaging, real-time imaging, synthetic aperture radar (SAR)

I. INTRODUCTION

Low-cost electromagnetic imaging systems have gained attention over the past decade as commercially available radar platforms have become increasingly affordable. Millimeter-wave (mmWave) radar has attracted exceptional interest for applications including gesture recognition [1], concealed threat detection [2], [3], and medical imaging [4], [5] due to its semi-penetrating non-ionizing nature and low power consumption. Additionally, with the emergence of fifth-generation (5G) and sixth-generation (6G) technology, ultra-wideband (UWB) mmWave transceivers are enabling unprecedented sensing and communications feats [6], [7].

Small form-factor multiple-input-multiple-output (MIMO) radars are increasing in popularity due to low cost and power consumption [1], [3]. Of particular interest, recent work has enabled freehand mmWave imaging by employing positioning sensors commonly employed in smartphones and virtual reality (VR) sensor suites [7]–[11]. Sub-wavelength localization accuracy was previously unachievable by conventional techniques such as 5G mmWave [12] or Bluetooth low energy (BLE) ranging [13]. Freehand mmWave imaging is a high-resolution imaging technique relying on conventional synthetic aperture radar (SAR) principles [14]–[18] and precise tracking of the handheld radar device as it is

moved by a human user throughout space [7], [19]–[21]. Whereas traditional mmWave SAR imaging requires precise motion systems to achieve near-ideal synthetic arrays [18], the scanning geometry employed by a freehand imaging system is generally irregular and does not conform to the typical array geometries required for efficient image reconstruction algorithms [22].

While recent work has proposed a fast imaging algorithm for irregular SAR geometries using array linearization [23], the proposed technique adopts a simplistic model of the array displacement and does not explore the near-field multistatic effects, both of which are addressed in this study. However, efficient algorithms for near-field MIMO-SAR operation under irregular scanning geometries are previously unexplored in the literature.

Extensive work on freehand mmWave imaging has been conducted by Laviada *et al.* at the University of Oviedo [7]–[11], [24], [25]. High-precision localization systems to enable freehand SAR imaging have been investigated using an infrared camera network to accurately track the device location across time and recover electromagnetic (EM) images [8]. Their work has been extended to employ an inertial measurement unit (IMU) and depth camera sensors to achieve standalone freehand imaging with promising results [7], [11]. In each of these efforts, the subject attempts to move the hand in a raster pattern to synthesize an approximately rectangular planar aperture [7]–[9]. Due to the subject's inability to move their hand in an ideal planar trajectory and the sensitivity of the mmWave signal to sub-millimeter perturbations, the image is reconstructed using the generalized back-projection algorithm (BPA).

Similar irregular and non-cooperative scanning geometries have been observed in unmanned aerial vehicle (UAV) SAR imaging [24], nonuniform NDT [25], and automotive SAR imaging [26]. However, for many edge and mobile applications, limitations on power consumption and computational complexity cannot be overcome by existing approaches for irregularly sampled SAR. Although image reconstruction algorithms have been thoroughly investigated in the literature for cooperative synthetic array geometries [1], [3], [14]–[18], [22], [27]–[32], widely applicable efficient near-field imaging algorithms for applications such as freehand smartphone imaging, UAV imaging, and automotive SAR imaging have not been thoroughly addressed in the existing literature. Furthermore, while MIMO arrays, commonly employed in commercially available radar devices, offer spatially efficient small array sizes, MIMO-SAR operation introduces a handful of complications to the image reconstruction process and proper handling of the multistatic array is necessary to avoid imaging artifacts [15]. While progress has been made towards projecting MIMO-SAR radar data to virtual single-input-single-output (SISO) monostatic data [15], [22], the analysis is performed on a coplanar assumption that does not generally hold for irregular scanning geometries.

In this article, we propose a novel image reconstruction technique for efficient near-field imaging with irregular scan-

ning geometries, such as those present in freehand imaging, UAV SAR, or automotive scenarios. We examine the system and signal models for UWB MIMO-SAR and develop a multi-planar multistatic approach to mathematically decompose the irregularly sampled synthetic array such that an equivalent virtual planar monostatic array can be constructed. The proposed algorithm is validated through simulation and experimentation, demonstrating robustness to arbitrary scanning patterns and offering low computational complexity. Our solution enables emerging technologies that require non-ideal SAR scanning geometries, MIMO multistatic radar, and efficient image reconstruction.

The remainder of this paper is organized as follows. Section II introduces the system model, including the multi-planar multistatic SAR concept, signal model, and a novel compensation technique to planar monostatic SAR. In Section III, efficient imaging methods and implementation details are discussed, and an enhanced algorithm is proposed. Section IV details the hardware and software implementation for collecting multi-planar multistatic SAR data. The results from the simulation and empirical studies are presented and discussed in Section V, followed by the conclusions.

II. SYSTEM MODEL

In this article, we propose the characterization of irregular or arbitrary three-dimensional (3-D) MIMO-SAR sampling geometry using the multi-planar multistatic scenario shown in Fig. 1, where data are collected along different z -planes by a MIMO multistatic radar with respect to a stationary 3-D target.

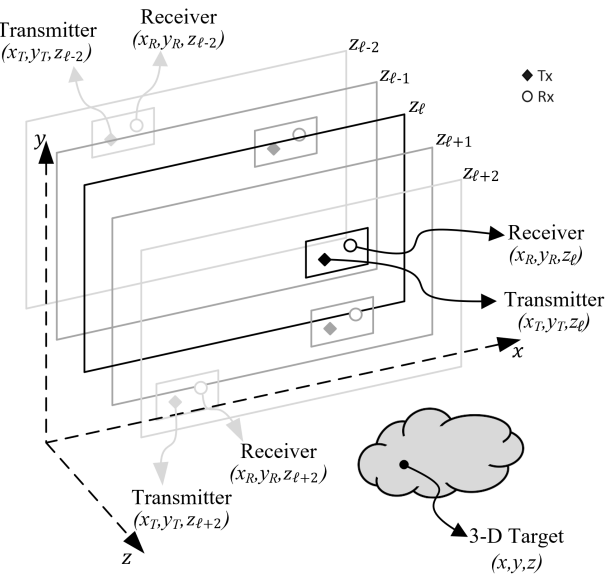


Figure 1: Geometry of the multi-planar SAR irregular scanning geometry with a multistatic array.

A. MULTI-PLANAR MIMO-SAR CONFIGURATION

For many SAR applications mentioned in Section I, as the radar is moved throughout 3-D space, it is generally oriented in the same direction towards some target; however, the samples are taken across several z -planes. As the data are collected while during an arbitrary SAR scanning path, the resulting synthetic aperture does not conform to the standard scanning regimes, for example, rectilinear/planar [2], [18], circular [25], [31], or cylindrical [14], [22], [32]. Hence, the image reconstruction process must consider the irregularity of the spatial sampling, whose geometry is detailed in Fig. 1.

B. THE 3-D MULTI-PLANAR VIRTUAL ARRAY RESPONSE IN NEAR-FIELD IMAGING

By the analysis of [15], [22], [33] for the 2-D case, a multistatic MIMO array can be approximated by a monostatic virtual element located at the midpoint of the transmit (Tx) and receive (Rx) elements under the far-field assumption for a small fraction ϵ as

$$\sqrt{(d_\ell^x)^2 + (d_\ell^y)^2} \leq \sqrt{4\epsilon\lambda R}, \quad (1)$$

where d_ℓ^x , d_ℓ^y are the distances between the Tx and Rx elements along the x - and y -directions, respectively, as shown in Fig. 2, λ is the wavelength of the carrier frequency, and R is the distance from the midpoint of the antenna elements to a reference point in the scene.

However, under the multi-planar multistatic framework, it is desirable to approximate each Tx/Rx pair by its virtual element located on a Z_0 plane in the near-field. In this way, multi-planar data can be projected onto a virtual planar array to ease the subsequent image reconstruction process. As shown in Fig. 2, the ℓ -th Tx/Rx pair located on the z_ℓ plane can be approximated by the element located at the midpoint between the Tx and Rx elements migrated to the Z_0 plane.

For near-field SAR, the assumption in (1) is not valid, and the approximation must be handled more delicately. Hence, we derive an efficient compensation algorithm to approximate the multistatic multi-planar array as a monostatic planar array for near-field imaging scenarios.

The transmitter (Tx) and receiver (Rx) of the ℓ -th multistatic MIMO array are located at (x_T, y_T, z_ℓ) and (x_R, y_R, z_ℓ) , respectively, and the target scene is assumed to be a distributed target whose coordinates are given by (x, y, z) . In this study, orthogonality is leveraged across time by operating the MIMO radar using the time-division-multiplexing (TDM) MIMO technique such that each Tx/Rx pair is activated sequentially. The round-trip distance between the ℓ -th Tx/Rx pair and the point scatterer located at (x, y, z) can be written as

$$\begin{aligned} R_\ell^{RT} &= R_\ell^T + R_\ell^R, \\ R_\ell^T &= [(x_T - x)^2 + (y_T - y)^2 + (z_\ell - z)^2]^{\frac{1}{2}}, \\ R_\ell^R &= [(x_R - x)^2 + (y_R - y)^2 + (z_\ell - z)^2]^{\frac{1}{2}}. \end{aligned} \quad (2)$$

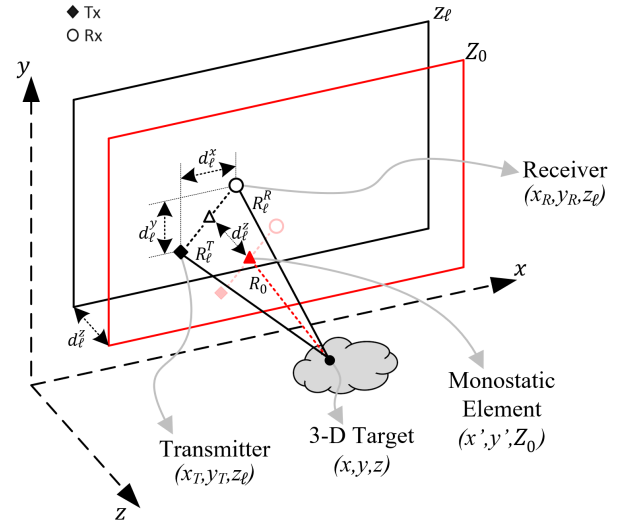


Figure 2: Relationship between the multi-planar multistatic elements and virtual planar monostatic elements.

Denoting virtual antenna element locations as (x', y', Z_0) , the x - and y -coordinates of the Tx/Rx pair can be expressed as

$$\begin{aligned} x_T &= x' - d_\ell^x/2, & y_T &= y' - d_\ell^y/2, \\ x_R &= x' + d_\ell^x/2, & y_R &= y' + d_\ell^y/2. \end{aligned} \quad (3)$$

Similarly, denoting d_ℓ^z as the distance between the Z_0 plane and the z_ℓ plane, as shown in Fig. 2, the z -coordinate of the Tx and Rx elements can be expressed with respect to Z_0 as

$$z_\ell = Z_0 + d_\ell^z. \quad (4)$$

As described in Appendix A, substituting (3) and (4) into (2) and applying the third order Taylor series expansion of R_ℓ for small values of d_ℓ^x , d_ℓ^y , and d_ℓ^z yields

$$\begin{aligned} R_\ell^{RT} &\approx 2R_0 + \frac{2(Z_0 - z)d_\ell^z}{R_0} + \frac{(d_\ell^x)^2 + (d_\ell^y)^2 + 4(d_\ell^z)^2}{4R_0} \\ &\quad - \frac{[(x' - x)d_\ell^x + (y' - y)d_\ell^y]^2 + 4(Z_0 - z)^2(d_\ell^z)^2}{4R_0^3}, \end{aligned} \quad (5)$$

where R_0 is the distance between the virtual monostatic element located at (x', y', Z_0) and the point scatterer at (x, y, z) , expressed as

$$R_0 = [(x' - x)^2 + (y' - y)^2 + (Z_0 - z)^2]^{\frac{1}{2}}. \quad (6)$$

Centering the target to the origin of the (x, y, z) coordinate system and considering $(x' - x), (y' - y) \ll Z_0$, we can acquire the improved approximation of the round-trip distance between the ℓ -th Tx/Rx pair and the point scatterer as

$$R_\ell^{RT} = R_\ell^T + R_\ell^R \approx 2R_0 + 2d_\ell^z + \frac{(d_\ell^x)^2 + (d_\ell^y)^2}{4Z_0}. \quad (7)$$

C. SIGNAL MODEL

Consider the multi-planar multistatic array whose Tx and Rx elements are located at (x_T, y_T, z_ℓ) and (x_R, y_R, z_ℓ) , respectively, and a distributed target occupying the volume V at locations (x, y, z) in 3-D space with a continuous reflectivity function given by $o(x, y, z)$. Without loss of generality, under the Born approximation for the scattering process and an isotropic antenna assumption, the received signal can be written as

$$\begin{aligned} s(x_T, x_R, y_T, y_R, z_\ell, t) \\ = \iiint_V \frac{o(x, y, z)}{R_\ell^T R_\ell^R} p \left(t - \frac{R_\ell^T}{c} - \frac{R_\ell^R}{c} \right) dx dy dz, \end{aligned} \quad (8)$$

where $p(t)$ is the transmitted signal, t is the fast-time variable, c is the speed of the EM wave, and R_ℓ^T, R_ℓ^R are given in (2).

The Fourier transform of (8) with respect to t yields the frequency spectrum as

$$\begin{aligned} s(x_T, x_R, y_T, y_R, z_\ell, f) \\ = P(f) \iiint_V \frac{o(x, y, z)}{R_\ell^T R_\ell^R} e^{-jk(R_\ell^T + R_\ell^R)} dx dy dz, \end{aligned} \quad (9)$$

where the instantaneous wavenumber $k = 2\pi f/c$ and $P(f)$ is the Fourier transform of $p(t)$. Image recovery requires the inversion of (9) to produce $o(x, y, z)$; however, given the arbitrary sampling locations, the image cannot be computed efficiently using existing techniques.

However, the derivation of (7) enables efficient compensation of multistatic multi-planar data by careful handling of the phase. To achieve the proposed compensation, we express the frequency response to the virtual planar monostatic array, whose elements are located at (x', y', Z_0) , as

$$\hat{s}(x', y', f) = P(f) \iiint_V \frac{o(x, y, z)}{R_0^2} e^{-j2kR_0} dx dy dz, \quad (10)$$

where R_0 is given by (6); x' and y' are the midpoints between each Tx/Rx pair; and Z_0 is the plane onto which the samples are projected. From the analysis in Section II-B, the relationship between the multi-planar multistatic response and virtual monostatic array response is given by

$$\hat{s}(x', y', f) \approx s(x_T, x_R, y_T, y_R, z_\ell, f) e^{jk\beta_\ell}, \quad (11)$$

where

$$\beta_\ell = 2d_\ell^z + \frac{(d_\ell^x)^2 + (d_\ell^y)^2}{4Z_0}, \quad (12)$$

is the near-field residual phase term due to the arbitrary scanning and MIMO effects in the near-field, as derived in (7). Hence, the virtual planar monostatic response can be efficiently acquired from the irregular samples by removing the residual phase to simultaneously account for multi-planar scanning geometry and near-field multistatic effects. The novel phase compensation technique derived in this section efficiently reduces the dimensionality of the MIMO-SAR imaging problem and projects multi-planar samples onto a single plane to enable computationally tractable algorithms for image reconstruction.

III. EFFICIENT IMAGE RECONSTRUCTION ALGORITHMS FOR NEAR-FIELD SAR

In this section, we review the traditional planar SAR image reconstruction methods using efficient Fourier-based solutions to recover EM images [22] and propose a novel technique for multi-planar multistatic SAR. Existing research on irregularly sampled SAR imaging problems employs the gold standard back-projection algorithm (BPA) [7]–[11], [24], [25]. However, this approach is computationally infeasible for many edge and mobile applications. To overcome this challenge, we employ the approximation in (11) to project multi-planar data to a planar-sampled scenario to satisfy the requirements for efficient image reconstruction. The Fourier-based algorithm detailed in the subsequent analysis is known as the range migration algorithm (RMA) or f - k algorithm and has been explored in greater detail elsewhere [16], [22], [27], [29], [30].

The key step to efficiently invert the integral in (10) is to represent the spherical wave term as a superposition of plane waves by the method of stationary phase (MSP) [15], [22], such that

$$\frac{e^{-j2kR_0}}{R_0} \approx \iint \frac{e^{-j(k'_x(x-x') + k'_y(y-y') + k_z(z-Z_0))}}{k_z} dk'_x dk'_y, \quad (13)$$

where

$$k_z^2 = 4k^2 - (k'_x)^2 - (k'_y)^2. \quad (14)$$

Following the analysis in [18], [22], substituting (13) into (10) and rearranging the phase terms to leverage the Fourier relationships yields

$$O(k_x, k_y, k_z) = \hat{S}(k'_x, k'_y, f) \frac{k_z}{P(f)} e^{-jk_z Z_0}, \quad (15)$$

where $O(k_x, k_y, k_z)$ and $\hat{S}(k'_x, k'_y, f)$ are the spatial spectral representations of the reflectivity function $o(\cdot)$ and array response $\hat{s}(\cdot)$, respectively. Since the primed and unprimed coordinate systems are coincident, the distinction can be dropped for the remaining analysis. Hence, the RMA image recovery process can be summarized as

$$\begin{aligned} o(x, y, z) = \\ \text{IFT}_{3D}^{(k_x, k_y, k_z)} \left[\mathcal{S} \left[\text{FT}_{2D}^{(x', y')} [\hat{s}(x', y', f)] \frac{k_z}{P(f)} e^{-jk_z Z_0} \right] \right], \end{aligned} \quad (16)$$

where $\text{FT}[\cdot]$ and $\text{IFT}[\cdot]$ are the forward and inverse Fourier transform operators, respectively, \mathcal{S} is the Stolt interpolation operator required to compensate for the spherical wavefront [22], and $\hat{s}(\cdot)$ is obtained from (11). The spatial resolution along each dimension of the recovered image is given by

$$\begin{aligned} \delta_x &= \frac{\lambda_c Z_0}{2D_x}, \\ \delta_y &= \frac{\lambda_c Z_0}{2D_y}, \\ \delta_z &= \frac{c}{2B}, \end{aligned} \quad (17)$$

where D_x and D_y are the size of the aperture along the x - and y -directions, respectively, B is the system bandwidth, and λ_c is the wavelength of the center frequency [15], [22], [29].

While (16) provides an efficient solution for planar array imaging problems, its application to irregular scanning geometries requires discussion of several key issues. Applying the compensation technique in (11) for irregularly sampled data, the multi-planar data can be approximately projected to planar sampling; however, they are likely non-uniform at the positions (x', y', Z_0) along the x - and y -directions. Traditional efficient implementations rely on the common fast Fourier transform (FFT) algorithm, but recent work on non-uniform planar MIMO-SAR [29], [30] and irregular MIMO real aperture radar (MIMO-RAR) [34] imaging has produced solutions using a non-uniform FFT (NUFFT) approach employing fast Gaussian gridding (FGG) discussed in [35] for the Fourier transforms and Stolt interpolation step in (16). The sampling criteria for the nonuniform planar case are discussed in detail in [29], [30], [34] and apply correspondingly to irregular scanning scenarios after multi-planar compensation. Similarly, the FGG-NUFFT technique is employed in this study to efficiently perform the RMA on irregularly sampled planar data.

For the multi-planar sampling scenario discussed in Section II-A, the RMA cannot be applied directly without multi-planar compensation because the data are sampled on different z -planes, as discussed in Section V. If the RMA is applied to the raw multi-planar data, the forward Fourier transform in (16) is invalid because the data along the x' and y' -directions are not coplanar and the resulting image will suffer from significant distortion, in most cases rendering the resulting images unusable.

Sampling considerations for image reconstruction remain identical to those in analyses elsewhere [15], [27], after the multi-planar compensation algorithm. While sampling criteria are not guaranteed for irregular SAR scanning if the relationship between the capture rate of the radar and the velocity of the radar platform is tuned appropriately during system design, undersampling artifacts are minimal in most cases [8]–[11].

In terms of computational complexity, our proposed algorithm offers a significant advantage over existing techniques in the literature [7]–[11], [24], [25], which employ the BPA, whose computational complexity is on the order of $O(N^6)$ [18], [30]. The time complexity of the RMA and its FGG-NUFFT variants are investigated in the literature [30], [34] and the multi-planar compensation step proposed in this article presents negligible computational expense to the RMA, which is on the order of $O(N^3 \log N)$ [17], [27]. Hence, as discussed in Section V, the algorithm proposed in this article offers comparable imaging performance to the BPA with tractable execution time for mobile platforms similar to the RMA.

The novel enhanced reconstruction process for efficient near-field SAR imaging with irregular scanning geometries is summarized in Fig. 3. Using the analysis in Section II,

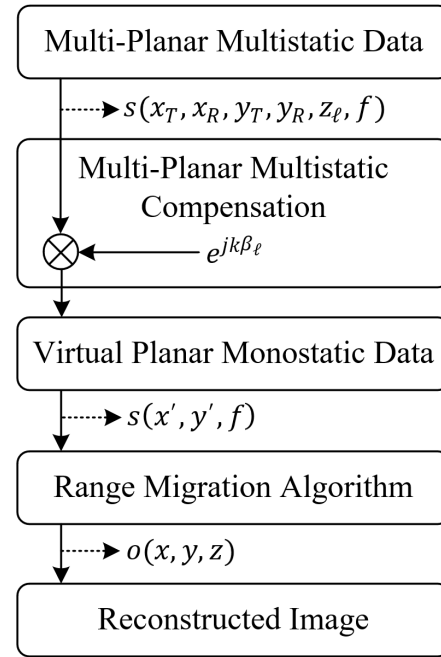


Figure 3: The complete image reconstruction process from irregular sampling compensation to RMA image recovery.

irregular scanning geometries can be modeled as multi-planar sampling scenarios, as shown in Fig. 1, and compensated by simply removing the residual phase due to the multi-planar multistatic conditions. Subsequently, virtual planar monostatic data are used to recover the image efficiently using the RMA. In simulation and empirical studies on irregular SAR scanning geometries, the proposed algorithm is applied to efficiently produce high-resolution 3-D images previously infeasible due to algorithmic deficiencies.

IV. MULTI-PLANAR MULTISTATIC IMAGING HARDWARE PROTOTYPE

In this section, we discuss the hardware prototype implementation for empirically validating the proposed imaging algorithm by collecting multi-planar multistatic SAR data. The hardware architecture of the mmWave imaging system is detailed in Fig. 4. A Texas Instruments (TI) mmWave MIMO radar is mounted on an x - y planar scanner. The TI AWR1443BOOST radar with 4 GHz bandwidth from 77 GHz to 81 GHz is mounted to a TI mmWave-Devpack and TSW1400 data capture card to store the data from the SAR scan and transfer it to the PC where the image recovery algorithm is implemented in MATLAB. The TI AWR1443BOOST is equipped with a MIMO array consisting of two Tx elements spaced by $2\lambda_c$ and four Rx elements spaced by $\lambda_c/2$ [15]. Additionally, a linear rail is used to move the target along the z -direction to collect multi-planar multistatic data under the geometry discussed in Section II-A. All three x - y - z rails are driven by stepper motors controlled by an AMC4030 motion controller, and the scanning process

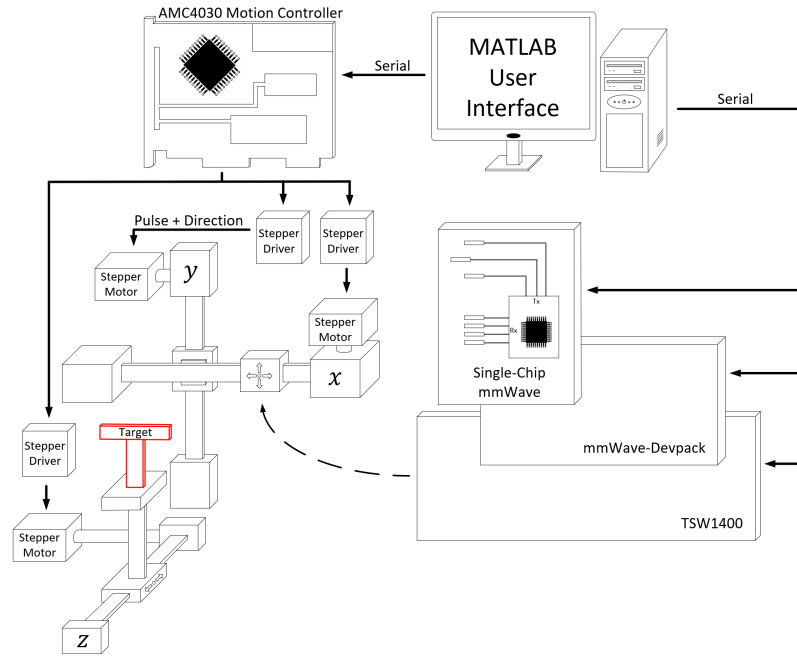


Figure 4: System design for 3-D scanner with radar mounted on planar x - y rails and target mounted on a linear z rail. The TI radar, data capture card, and mechanical scanner are controlled by MATLAB via USB serial interface.

and radar set up are handled in MATLAB. Additional details on system development and device calibration can be found in [18]. The images are reconstructed using MATLAB implementations running on a desktop PC equipped with a 12-core AMD Ryzen 9 3900X running at 4.6 GHz with 64 GB of memory. Using this hardware prototype, data can be collected for many target scenarios under the multi-planar multistatic scenario by performing multiple planar SAR scans with the target at different z -locations. To emulate irregular scanning geometries, the data collected throughout x - y - z space are subsampled, as discussed in Section V. Implementations in the literature employ multi-camera infrared camera systems to track the radar as it is moved through space by the user [8], [9]. Other studies on irregular scanning geometries have explored freehand imaging using a stereo camera with an IMU for positioning estimation [7] and UAV near-field imaging with a laser rangefinder and real-time kinematic (RTK) system for localization [24]. These implementations, among others [10], [11], [25], [26], demonstrate the viability of high-resolution sensors for precise positioning to enable novel imaging techniques using UWB mmWave radar. Hence, this study focuses on improving the computational efficiency of the imaging technique and assumes that the position of the radar is known across the irregularly sampled geometry.

V. MEASUREMENT AND IMAGING RESULTS

In this section, we validate the proposed algorithm derived in Sections II and III, and shown in Fig. 3. Irregular scanning geometries are simulated using the simulation platform developed in [22], and image reconstruction results are shown

comparing our enhanced method to the gold standard BPA and RMA without multi-planar multistatic compensation. Similarly, using the 3-D mechanical system detailed in Fig. 4, irregular scanning geometries are emulated by collecting planar scans with the target at different z -locations and subsampling the collected data. Imaging results are provided comparing the proposed algorithm against the BPA and RMA, demonstrating the computational advantage of our technique. The proposed multi-planar multistatic compensation algorithm achieves image quality comparable to that of the BPA while offering time and space complexity on par with the RMA.

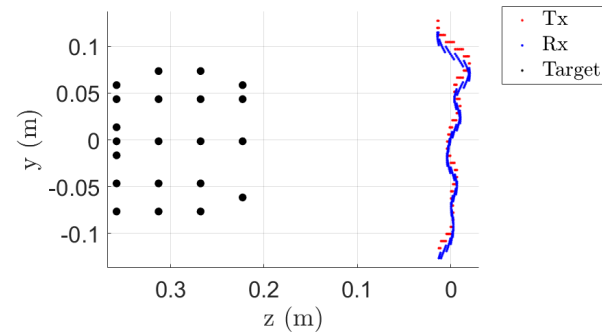


Figure 5: Irregular scanning geometry for “UTD” scenario consisting of a multi-linear array in the y -direction at $x = 0$ m.

A. SIMULATED SAR IMAGING RESULTS

To validate our proposed algorithm in simulation, we consider two scenarios. First, a linear array along the y -axis is simulated as shown in Fig. 5 with 21 point scatterers arranged as the letters “UTD”. The irregular array locations are generated by a semi-smooth, random curve spanning $y' \in [-12.5, 12.5]$ cm and $z_\ell \in [-2.5, 2.5]$ cm. As shown in Fig. 6a, the gold standard BPA recovers each point scatterer without artifacts; however, computing the BPA image requires 296.3 s on our machine. The RMA without multi-planar multistatic compensation and the proposed algorithm are considerably more efficient, requiring only 30 ms for computation. However, while the RMA image in Fig. 6b is significantly distorted and the image is lost, our proposed method resolves the point targets comparably to the BPA and requires a fraction of the computation time.

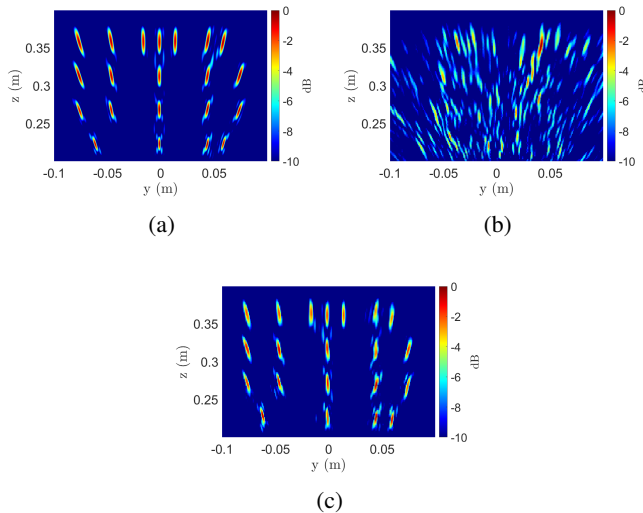


Figure 6: Imaging results for the scenario in Fig. 5 using the (a) BPA (296.3 s), (b) RMA without multi-planar multistatic compensation (29 ms), and (c) our proposed algorithm (30 ms).

Considering the more broadly applicable 2-D scanning case, a 2-D multi-planar multistatic scenario is simulated with a solid target located at $z = 300$ mm, as shown in Fig. 7. The target is a rectangular strip with cutouts of various sizes and the irregular sampling geometry is generated as a 2-D semi-smooth random curve occupying $x' \in [-12.5, 12.5]$ cm, $y' \in [-12.5, 12.5]$ cm, and $z_\ell \in [-2.5, 2.5]$ cm. Since the target is located on a single z -plane parallel to the planar projection after our compensation technique, a 2-D x - y image is recovered at $z = 300$ mm. Again, while the BPA yields a robust reconstruction, the computation time is excessive for most applications, requiring 1324.8 s on a desktop machine. On the other hand, the proposed algorithm outperforms the RMA significantly in terms of image quality, nearly matching that of the BPA with only slight artifacting, while demonstrating superior efficiency to the BPA computing a high-resolution 2-D image

in only 1.1 s. Similarly, 3-D images can be reconstructed using these methods. The 3-D reconstructed image using the proposed algorithm is shown in Fig. 8d, requiring 4.8 s to compute, while the RMA and BPA are computed in 4.8 s and 339159.2 s, respectively.

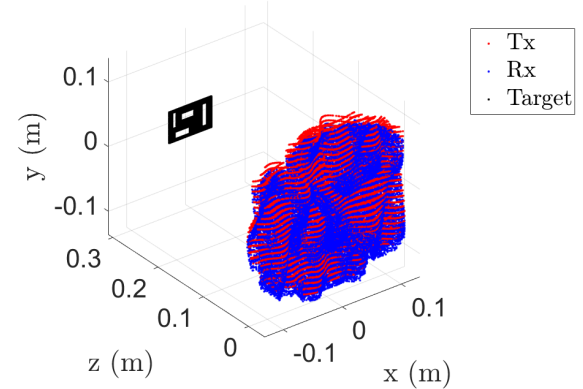


Figure 7: Irregular scanning geometry for cutout consisting of a multi-planar array along the x - y -directions.

Comparing the results from Figs. 6 and 8, aberrations appear more pronounced along the z -dimension or depth. This phenomenon is to be expected given the analysis in Section II-B, where d_ℓ^z and the size of the target in the z -direction are assumed to be small. Hence, for targets of significant size in the z -direction, such as the target in Fig. 6b, the proposed compensation suffers from slight artifacting compared with the BPA. However, for many applications, the considerable time savings achieved using our technique is a necessary trade-off compared to the prohibitively slow BPA.

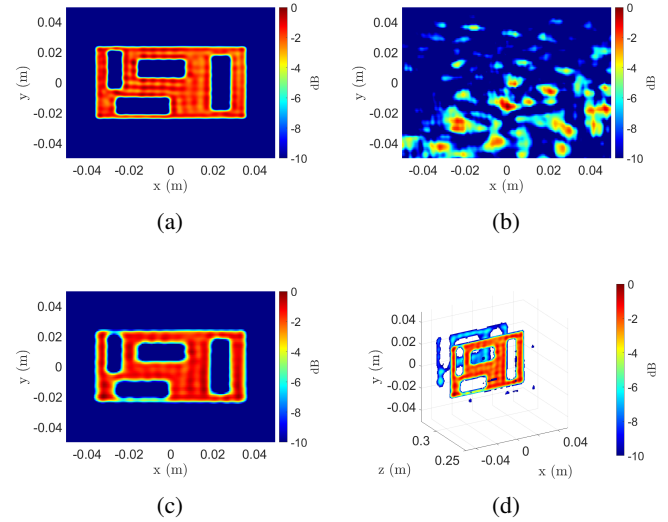


Figure 8: Imaging results for the scenario in Fig. 7 using the (a) BPA (1324.8 s), (b) RMA without multi-planar multistatic compensation (1.1 s), (c) proposed algorithm at the $z = 300$ mm plane (1.1 s), and (d) the 3-D reconstructed image using the proposed technique (4.8 s).

B. EMPIRICAL IRREGULAR GEOMETRY SAR IMAGING RESULTS

The multi-planar multistatic imaging technique and system prototype are validated experimentally by capturing SAR data of various target scenes, shown in Fig. 9. The reconstructed images obtained using each method are compared and discussed.

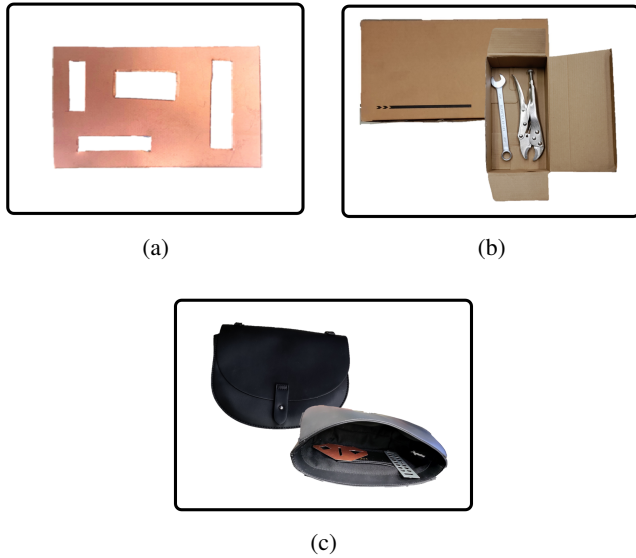


Figure 9: Various experimental targets: (a) copper clad laminate test target, (b) tools hidden inside box, and (c) purse containing metal cutouts.

The test target with several horizontal and vertical rectangular cutouts made from copper-clad laminate (Fig. 9a) is illuminated by the x - y scanner at the planes $z \in [275, 324]$ mm with a separation of 1 mm. Hence, data are collected throughout the same region discussed previously such that $x' \in [-12.5, 12.5]$ cm, $y' \in [-12.5, 12.5]$ cm, and $z_\ell \in [-2.5, 2.5]$ cm. After the data were collected, the 50 planar scans were subsampled using a similar random 2-D curves as shown in Fig. 7s to emulate the multi-planar irregular sampling scenario. The imaging results and the corresponding computation times for each reconstruction algorithm are shown in Fig. 10. Our proposed multi-planar multistatic imaging technique demonstrates robustness in projecting the irregular scanning geometry to a planar scenario for more efficient image recovery as the cutout is recovered cleanly without significant artifacting, as shown in Fig. 10c. In contrast, the image recovered using the BPA requires nearly 30 minutes to compute, and although the RMA is computed efficiently, the RMA without multi-planar compensation is unable to resolve the target scene, as shown in Fig. 10b. Furthermore, when the target location is unknown in the z -direction, 3-D imaging offers an improved solution at a higher computational cost.

The second target screened by the prototype to demonstrate a hidden target scenario consists of two wrenches (a combination wrench and a vise grip) hidden inside a card-

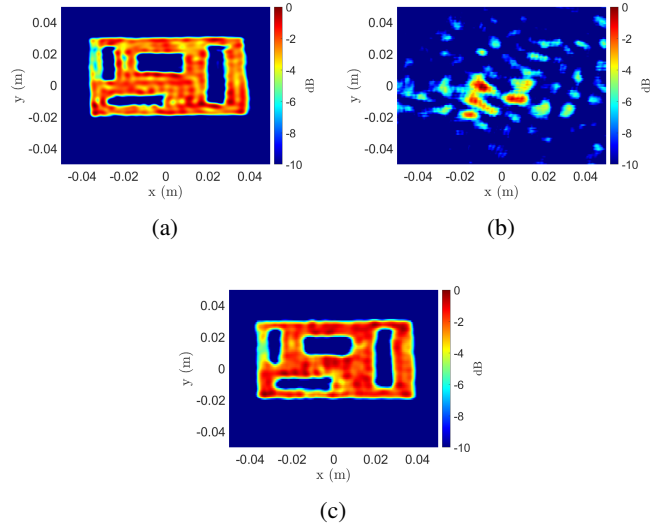


Figure 10: Imaging results for the copper test target using the (a) BPA (1324.8 s), (b) RMA without multi-planar multistatic compensation (1.1 s), and (c) proposed algorithm (1.1 s).

board box, as shown in Fig. 9b. SAR scans of the target are performed with the target at the z -planes $z \in [275, 324]$ mm with a separation of 1 mm. To accommodate a larger target size, the aperture is increased to $x' \in [-25, 25]$ cm, $y' \in [-25, 25]$ cm, and $z_\ell \in [-2.5, 2.5]$ cm. Similarly, the x - y - z data are sampled to emulate the multi-planar multistatic scenario using a semi-smooth random curve as shown in Fig. 7. The 2-D and 3-D implementations of the BPA and proposed algorithm are applied to the nonuniform data under the irregular scanning geometry, and the recovered images are shown in Fig. 11. Both wrenches are visible in the reconstructed images; however, while the 2-D image from the BPA and proposed algorithm provide high-fidelity reconstructions of the hidden tools, the 2-D z -plane must be carefully selected to obtain such images. The presence and location of targets are generally unknown for concealed item detection problems such as this. Hence, 3-D imaging is preferable for such scenarios and is primarily constrained by computational expense. Our proposed algorithm offers an elegant compromise between the efficiency of the RMA and the image quality of the BPA. In Fig. 11d, the 3-D image is computed by the proposed algorithm with an image quality comparable to that of the BPA with significantly reduced computational cost.

A third experiment is conducted with several metal cutouts concealed in a purse to emulate a scenario wherein a suspicious personal item is quickly screened with an irregular scanning geometry, such as freehand SAR or drone imaging. Fig 9c shows the purse and two hidden items: one triangularly shaped metal plate with different cutout shapes and one rectangular metal plate with circular holes. The target is scanned by the multi-planar multistatic prototype discussed in Section IV, and the

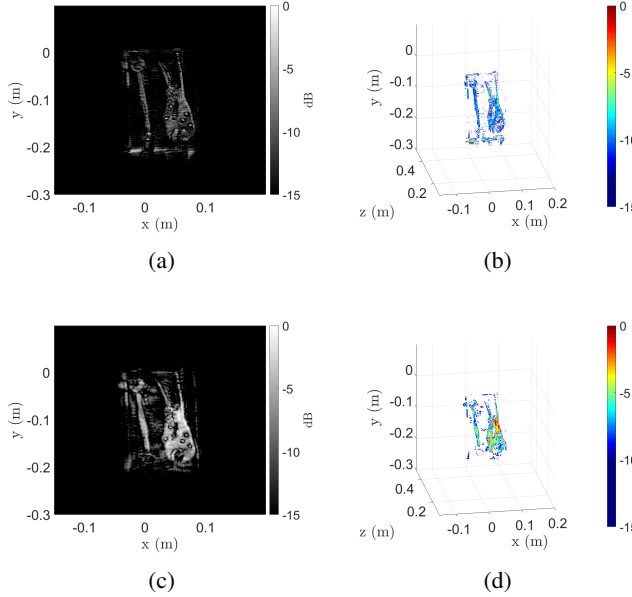


Figure 11: Imaging results for the hidden tools target, as shown in Fig. 9b, using the (a) 2-D BPA (5299.4 s), (b) 3-D BPA (1356636.9 s), (c) 2-D proposed algorithm (4.3 s), and (d) 3-D proposed algorithm (10.7 s).

data are employed to emulate an irregular sampling scenario. Scans are performed with the target at the z -planes $z \in [275, 324]$ mm with a separation of 1 mm and an aperture is synthesized within $x' \in [-25, 25]$ cm, $y' \in [-25, 25]$ cm, and $z_\ell \in [-2.5, 2.5]$ cm. The reconstructed images and the corresponding computation times are shown in Fig. 12. Both metal cutouts are resolved using our algorithm with image quality comparable to that of the BPA. Again, assuming that the contents of the purse are generally unknown, computing the 3-D image is preferable for concealed item detection. To efficiently recover a 3-D image with irregularly sampled data, existing inversion techniques require excessive computation time and memory capacity, as shown in Figs. 12a and 12b. However, our proposed algorithm (Figs. 12c and 12d) offers an efficient solution that does not compromise image quality.

These experiments demonstrate the advantages of the proposed algorithm and the limitations of the RMA and BPA. A comparison of the required computation times for each algorithm is presented in Table 1. Applying the RMA directly to the multi-planar data, as shown in Figs. 6b, 8b, and 10b, yields significant aberrations to the point of failed reconstruction. For this reason, the RMA images are not shown for the other examples. When the target is known to be 2-D and located at a single, known z -plane, the 2-D BPA implementation can be computed somewhat efficiently in certain instances by employing a graphics processing unit (GPU) and parallelizing the computation [7]–[11]. However, particularly for mobile applications, access to high-capacity GPUs is rare or size-prohibitive, and such acceleration is infeasible. Moreover, as the BPA is scaled up to three dimensions, the

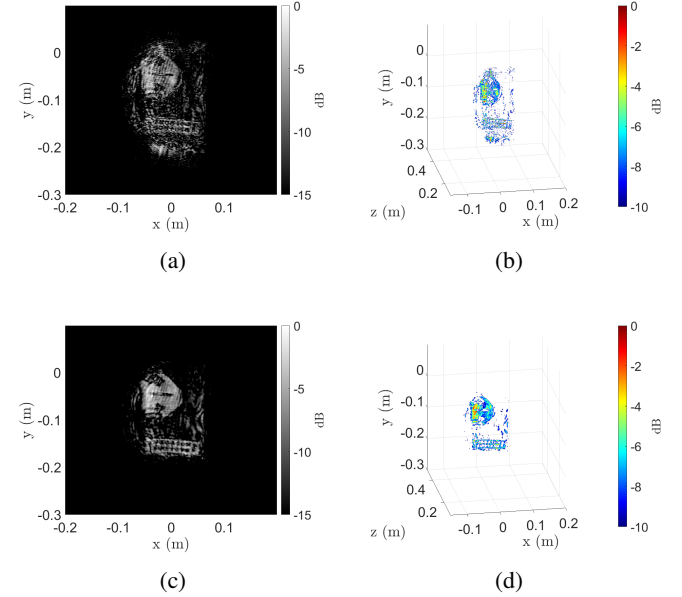


Figure 12: Imaging results for the concealed items in a purse, as shown in Fig. 9c, using the (a) 2-D BPA (5299.4 s), (b) 3-D BPA (1356636.9 s), (c) 2-D proposed algorithm (4.3 s), and (d) 3-D proposed algorithm (10.7 s).

time and space complexities increase exponentially, requiring excessive computational power and memory. In many emerging applications, efficient 3-D image computation on low-power devices is preferable, if not mandatory, as the precise location of the target is generally unknown. However, efficient algorithms, such as the RMA, require monostatic, planar assumptions that are unachievable by these applications. To enable such technologies, our proposed multi-planar multistatic imaging algorithm efficiently compensates for the irregular scanning geometry by careful handling of the phase of each sample. This enables image reconstruction under dynamic conditions with identical computational complexity to the RMA and image quality comparable to that of the BPA.

	Metal Cutout	Hidden Tools	Purse
2-D BPA	1324.8	5299.4	5299.4
3-D BPA	339159.2	1356636.9	1356636.9
2-D RMA	1.1	4.3	4.3
3-D RMA	4.8	10.7	10.7
2-D Proposed	1.1	4.3	4.3
3-D Proposed	4.8	10.7	10.7

Table 1: Computation time, in seconds, required by the various algorithms for each experiment.

VI. CONCLUSION

In this article, we presented a novel approach for high-resolution, efficient 3-D near-field SAR imaging for irregular scanning geometries. We proposed a multi-planar multistatic framework applicable to a diverse set of applications, including freehand imaging, UAV SAR, and automotive imaging. A novel algorithm is proposed to efficiently compensate

irregularly sampled multi-planar multistatic data to equivalent planar monostatic mmWave radar data. Simulation results are presented demonstrating the robustness of our approach in the presence of significant deviation among samples along the z -direction. Furthermore, we empirically validated the proposed algorithm using a custom prototype to capture multi-planar multistatic data for several concealed and obscured scenarios. In both simulation and experimental studies, our algorithm achieves efficient image reconstruction matching the focusing quality of the existing techniques while reducing computational complexity by a considerable margin.

APPENDIX A MULTIVARIATE TAYLOR SERIES EXPANSION

Consider an infinitely differentiable real-valued function and an open neighborhood around $(u, v, w) = (u_0, v_0, w_0)$. Let $\mathbf{x} = [u \ v \ w]^T$ and $\mathbf{x}_0 = [u_0 \ v_0 \ w_0]^T$. Hence, the multivariate Taylor series expansion of $f(\mathbf{x})$ in the neighborhood of \mathbf{x}_0 can be written as

$$f(\mathbf{x}) = f(\mathbf{x}_0) + (\mathbf{x} - \mathbf{x}_0)^T \nabla f(\mathbf{x}_0) + \frac{1}{2!} (\mathbf{x} - \mathbf{x}_0)^T \mathbf{H}(\mathbf{x}_0) (\mathbf{x} - \mathbf{x}_0) + \dots, \quad (18)$$

where ∇f is the vector of first derivatives

$$\nabla f(\mathbf{x}) = \begin{bmatrix} f_u(\mathbf{x}) \\ f_v(\mathbf{x}) \\ f_w(\mathbf{x}) \end{bmatrix}, \quad (19)$$

and $\mathbf{H}(\mathbf{x})$ is the Hessian matrix of the second derivatives as

$$\mathbf{H}(\mathbf{x}) = \begin{bmatrix} f_{uu}(\mathbf{x}) & f_{uv}(\mathbf{x}) & f_{uw}(\mathbf{x}) \\ f_{vu}(\mathbf{x}) & f_{vv}(\mathbf{x}) & f_{vw}(\mathbf{x}) \\ f_{wu}(\mathbf{x}) & f_{wv}(\mathbf{x}) & f_{ww}(\mathbf{x}) \end{bmatrix}. \quad (20)$$

A. TAYLOR SERIES EXPANSION OF ROUND-TRIP DISTANCE FOR IRREGULAR SCANNING GEOMETRIES

The round-trip distance between the ℓ -th Tx/Rx pair, whose transmitter and receiver elements are located at (x_T, y_T, z_ℓ) and (x_R, y_R, z_ℓ) , respectively, and the scatterer located at (x, y, z) is expressed in (2). Substituting (3) and (4) into (2), R_ℓ^{RT} can be expressed as a function of the distances between the Tx and Rx elements along the x - and y -directions, d_ℓ^x and d_ℓ^y , respectively, and displacement along the z -direction, d_ℓ^z :

$$R_\ell^{RT}(d_\ell^x, d_\ell^y, d_\ell^z) = \left[(x' - \frac{d_\ell^x}{2} - x)^2 + (y' - \frac{d_\ell^y}{2} - y)^2 + (Z_0 + d_\ell^z - z)^2 \right]^{\frac{1}{2}} + \left[(x' + \frac{d_\ell^x}{2} - x)^2 + (y' + \frac{d_\ell^y}{2} - y)^2 + (Z_0 + d_\ell^z - z)^2 \right]^{\frac{1}{2}}. \quad (21)$$

The first derivatives of (21), evaluated at $d_\ell^x = d_\ell^y = d_\ell^z = 0$, are

$$\begin{aligned} \frac{\partial R_\ell^{RT}}{\partial d_\ell^x} \Big|_{(d_\ell^x=d_\ell^y=d_\ell^z=0)} &= \frac{\partial R_\ell^{RT}}{\partial d_\ell^y} \Big|_{(d_\ell^x=d_\ell^y=d_\ell^z=0)} = 0, \\ \frac{\partial R_\ell^{RT}}{\partial d_\ell^y} \Big|_{(d_\ell^x=d_\ell^y=d_\ell^z=0)} &= \frac{2(Z_0 - z)}{R_0}, \end{aligned} \quad (22)$$

where R_0 is the distance between the virtual monostatic element located at (x', y', Z_0) and the point scatterer at (x, y, z) , expressed in (6).

The second derivatives of (21), evaluated at the point of interest, can be derived as

$$\begin{aligned} \frac{\partial^2 R_\ell^{RT}}{\partial(d_\ell^x)^2} \Big|_{(d_\ell^x=d_\ell^y=d_\ell^z=0)} &= \frac{1}{2R_0} \left[1 - \frac{(x' - x)^2}{R_0^2} \right], \\ \frac{\partial^2 R_\ell^{RT}}{\partial(d_\ell^y)^2} \Big|_{(d_\ell^x=d_\ell^y=d_\ell^z=0)} &= \frac{1}{2R_0} \left[1 - \frac{(y' - y)^2}{R_0^2} \right], \\ \frac{\partial^2 R_\ell^{RT}}{\partial(d_\ell^z)^2} \Big|_{(d_\ell^x=d_\ell^y=d_\ell^z=0)} &= \frac{2}{R_0} \left[1 - \frac{(Z_0 - z)^2}{R_0^2} \right], \\ \frac{\partial^2 R_\ell^{RT}}{\partial d_\ell^x d_\ell^y} \Big|_{(d_\ell^x=d_\ell^y=d_\ell^z=0)} &= -\frac{(x' - x)(y' - y)}{2R_0^3}, \\ \frac{\partial^2 R_\ell^{RT}}{\partial d_\ell^x d_\ell^z} \Big|_{(d_\ell^x=d_\ell^y=d_\ell^z=0)} &= \frac{\partial^2 R_\ell^{RT}}{\partial d_\ell^y d_\ell^z} \Big|_{(d_\ell^x=d_\ell^y=d_\ell^z=0)} = 0. \end{aligned} \quad (23)$$

Substituting (22) and (23) into (18), the quadratic approximation of R_ℓ can be expressed as

$$R_\ell^{RT} \approx 2R_0 + \frac{2(Z_0 - z)d_\ell^z}{R_0} + \frac{(d_\ell^x)^2 + (d_\ell^y)^2 + 4(d_\ell^z)^2}{4R_0} - \frac{[(x' - x)d_\ell^x + (y' - y)d_\ell^y]^2 + 4(Z_0 - z)^2(d_\ell^z)^2}{4R_0^3}. \quad (24)$$

References

- [1] J. W. Smith, O. Furxhi, and M. Torlak, "An FCNN-based super-resolution mmWave radar framework for contactless musical instrument interface," *IEEE Trans. Multimedia*, pp. 1–1, May 2021.
- [2] D. M. Sheen, T. E. Hall, D. L. McMakin, A. M. Jones, and J. R. Tedeschi, "Three-dimensional radar imaging techniques and systems for near-field applications," in *Proc. SPIE 9829 Radar Sensor Techn. XX*, Baltimore, MD, USA, May 2016, pp. 230–241.
- [3] M. E. Yanik and M. Torlak, "Near-field 2-D SAR imaging by millimeter-wave radar for concealed item detection," in *Proc. IEEE RWS*, Orlando, FL, USA, Jan. 2019, pp. 1–4.
- [4] L. Chao, M. N. Afsar, and K. A. Korolev, "Millimeter wave dielectric spectroscopy and breast cancer imaging," in *Proc. IEEE EuMIC*, Amsterdam, Netherlands, Oct. 2012, pp. 572–575.
- [5] Y. Gao and R. Zoughi, "Millimeter wave reflectometry and imaging for noninvasive diagnosis of skin burn injuries," *IEEE Trans. Instrum. Meas.*, vol. 66, no. 1, pp. 77–84, Nov. 2016.

- [6] O. Li, J. He, K. Zeng, *et al.*, “Integrated sensing and communication in 6G a prototype of high resolution THz sensing on portable device,” in *Proc. IEEE EuCNC/6G*, Porto, Portugal, Jun. 2021, pp. 544–549.
- [7] G. Álvarez-Narciandi, J. Laviada, and F. Las-Heras, “Towards turning smartphones into mmWave scanners,” *IEEE Access*, vol. 9, pp. 45 147–45 154, Mar. 2021.
- [8] G. Álvarez-Narciandi, M. López-Portugués, F. Las-Heras, and J. Laviada, “Freehand, agile, and high-resolution imaging with compact mm-Wave radar,” *IEEE Access*, vol. 7, pp. 95 516–95 526, Jul. 2019.
- [9] G. Álvarez-Narciandi, J. Laviada, and F. Las-Heras, “Freehand mm-Wave imaging with a compact MIMO radar,” *IEEE Trans. Antennas Propag.*, vol. 69, no. 2, pp. 1224–1229, Feb. 2021.
- [10] G. Álvarez-Narciandi, J. Laviada, Y. Álvarez-López, *et al.*, “Freehand system for antenna diagnosis based on amplitude-only data,” *IEEE Trans. Antennas Propag.*, vol. 69, no. 8, pp. 4988–4998, Feb. 2021.
- [11] H. F. Álvarez, G. Álvarez-Narciandi, F. Las-Heras, and J. Laviada, “System based on compact mmWave radar and natural body movement for assisting visually impaired people,” *IEEE Access*, vol. 9, pp. 125 042–125 051, Sep. 2021.
- [12] H. Wymeersch, G. Seco-Granados, G. Destino, D. Dardari, and F. Tufvesson, “5G mmWave positioning for vehicular networks,” *IEEE Wireless Commun.*, vol. 24, no. 6, pp. 80–86, Dec. 2017.
- [13] Z. Hajiakhondi-Meybodi, M. Salimibeni, K. N. Plataniotis, and A. Mohammadi, “Bluetooth low energy-based angle of arrival estimation via switch antenna array for indoor localization,” in *Proc. IEEE FUSION*, Rustenburg, South Africa, Jul. 2020, pp. 1–6.
- [14] J. W. Smith, M. E. Yanik, and M. Torlak, “Near-field MIMO-ISAR millimeter-wave imaging,” in *Proc. IEEE RadarConf*, Florance, Italy, Sep. 2020, pp. 1–6.
- [15] M. E. Yanik and M. Torlak, “Near-field MIMO-SAR millimeter-wave imaging with sparsely sampled aperture data,” *IEEE Access*, vol. 7, pp. 31 801–31 819, Mar. 2019.
- [16] M. E. Yanik, D. Wang, and M. Torlak, “3-D MIMO-SAR imaging using multi-chip cascaded millimeter-wave sensors,” in *Proc. IEEE GlobalSIP*, Ottawa, ON, Canada, Nov. 2019, pp. 1–5.
- [17] J. M. Lopez-Sanchez and J. Fortuny-Guasch, “3-D radar imaging using range migration techniques,” *IEEE Trans. Antennas Propag.*, vol. 48, no. 5, pp. 728–737, May 2000.
- [18] M. E. Yanik, D. Wang, and M. Torlak, “Development and demonstration of MIMO-SAR mmWave imaging testbeds,” *IEEE Access*, vol. 8, pp. 126 019–126 038, Jul. 2020.
- [19] C. F. Baumgartner, K. Kamnitsas, J. Matthew, *et al.*, “SonoNet: Real-time detection and localisation of fetal standard scan planes in freehand ultrasound,” *IEEE Trans. Medical Imaging*, vol. 36, no. 11, pp. 2204–2215, Jul. 2017.
- [20] J. Blackall, G. Penney, A. King, and D. Hawkes, “Alignment of sparse freehand 3-D ultrasound with preoperative images of the liver using models of respiratory motion and deformation,” *IEEE Trans. Medical Imaging*, vol. 24, no. 11, pp. 1405–1416, Oct. 2005.
- [21] M. W. Gilbertson and B. W. Anthony, “Force and position control system for freehand ultrasound,” *IEEE Trans. Robotics*, vol. 31, no. 4, pp. 835–849, Jun. 2015.
- [22] J. Smith and M. Torlak, “Terhertz imaging toolbox with interactive user interface,” *unpublished*, 2022.
- [23] X. Zeng, Y. Ma, Z. Li, J. Wu, and J. Yang, “A near-field fast time-frequency joint 3-D imaging algorithm based on aperture linearization,” in *Proc. IEEE IGARSS*, Brussels, Belgium, Oct. 2021, pp. 5163–5166.
- [24] M. Garcia-Fernandez, Y. Alvarez-Lopez, and F. L. Heras, “3D-SAR processing of UAV-mounted GPR measurements: Dealing with non-uniform sampling,” in *Proc. IEEE EuCAP*, Copenhagen, Denmark, Aug. 2020, pp. 1–5.
- [25] B. Wu, G. Álvarez-Narciandi, and J. Laviada, “Multilayered circular dielectric structure SAR imaging using time-reversal compressed sensing algorithms based on nonuniform measurement,” *IEEE Antennas Wireless Propag. Lett.*, vol. 19, no. 9, pp. 1491–1495, 2020.
- [26] T. Kan, G. xin, L. xiaowei, and L. zhongshan, “Implementation of real-time automotive SAR imaging,” in *Proc. IEEE SAM*, Hangzhou, China, Jun. 2020, pp. 1–4.
- [27] D. M. Sheen, D. L. McMakin, and T. E. Hall, “Three-dimensional millimeter-wave imaging for concealed weapon detection,” *IEEE Trans. Microw. Theory Techn.*, vol. 49, no. 9, pp. 1581–1592, Sep. 2001.
- [28] J. W. Smith, S. Thiagarajan, R. Willis, Y. Makris, and M. Torlak, “Improved static hand gesture classification on deep convolutional neural networks using novel sterile training technique,” *IEEE Access*, vol. 9, pp. 10 893–10 902, Jan. 2021.
- [29] J. Gao, Y. Qin, B. Deng, H. Wang, and X. Li, “Novel efficient 3D short-range imaging algorithms for a scanning 1D-MIMO array,” *IEEE Trans. Image Process.*, vol. 27, no. 7, pp. 3631–3643, Apr. 2018.
- [30] B. Fan, J. Gao, H. Li, Z. Jiang, and Y. He, “Near-field 3D SAR imaging using a scanning linear MIMO array with arbitrary topologies,” *IEEE Access*, vol. 8, pp. 6782–6791, Dec. 2019.
- [31] J. Gao, B. Deng, Y. Qin, H. Wang, and X. Li, “Efficient terahertz wide-angle NUFFT-based inverse synthetic aperture imaging considering spherical wavefront,” *Sensors*, vol. 16, no. 12, p. 2120, Dec. 2016.
- [32] R. K. Amineh, N. K. Nikolova, and M. Ravan, *Real-Time Three-Dimensional Imaging of Dielectric Bodies*

- Using Microwave/Millimeter Wave Holography.* John Wiley & Sons, 2019.
- [33] J. H. G. Ender and J. Klare, "System architectures and algorithms for radar imaging by MIMO-SAR," in *Proc. IEEE RadarConf*, Pasadena, CA, USA, May 2009, pp. 1–6.
 - [34] J. Wang, P. Aubry, and A. Yarovoy, "3-D short-range imaging with irregular MIMO arrays using NUFFT-based range migration algorithm," *IEEE Trans. Geosci. Remote Sens.*, vol. 58, no. 7, pp. 4730–4742, Jan. 2020.
 - [35] L. Greengard and J.-Y. Lee, "Accelerating the nonuniform fast Fourier transform," *SIAM Rev.*, vol. 46, no. 3, pp. 443–454, 2004.



JOSIAH W. SMITH (S'18) was born in Denver, CO, USA in 1997. He received the B.S. degree (*summa cum laude*) in electrical engineering from The University of Texas at Dallas in 2019, where he is currently pursuing a Ph.D. degree in electrical engineering specializing in communications engineering. He was awarded the Texas Instruments Analog Excellence Graduate Fellowship in August 2019 and the Louis Beecherl, Jr. Graduate Research Fellowship in August 2021. During the summer of 2020, he developed real-time human-computer interaction algorithms for mmWave radar with imec-USA. In the summer of 2021, he developed advanced deep learning and data-driven algorithms for user experience enhancement at Apple in the Display Technologies group. His current research interests include hybrid-learning algorithms, new regime radar imaging algorithm development, ultra-wideband radar imaging algorithms, terahertz radar, radar perception, computer vision, deep learning, millimeter-wave sensing, and phased array signal processing.



MURAT TORLAK (SM'04) received the M.S. and Ph.D. degrees in electrical engineering from The University of Texas at Austin, in 1995 and 1999, respectively. Since August 1999, he has been with the Department of Electrical and Computer Engineering, The University of Texas, where he has been promoted to the rank of a Full Professor. He is serving as a Rotating Program Director at the U.S. National Science Foundation (NSF). His current research interests include experimental verification of wireless networking systems, cognitive radios, millimeter-wave automotive radars, millimeter-wave imaging systems, and interference mitigation in radio telescopes. He was the General Chair of Symposium on Millimeter Wave Imaging and Communications in the 2013 IEEE GlobalSIP Conference. He has served as an Associate Editor for the IEEE Transactions on Wireless Communications, from 2008 to 2013. He is a Guest co-Editor of IEEE JSTSP Special Issue on Recent Advances in Automotive Radar Signal Processing, 2021.

• • •